Raman scattering study of the ferroelectric phase transition in $BaTi_2O_5$

Shinya Tsukada,[1,*] Yasuhiro Fujii,[2,†] Yasuhiro Yoneda,[3] Hiroki Moriwake,[4,5] Ayako Konishi,[4] and Yukikuni Akishige[6]

[1]*Faculty of Education, Shimane University, Matsue 690-8504, Japan*

[2]*Department of Physical Sciences, College of Science and Engineering, Ritsumeikan University, Kusatsu, Shiga 525-8577, Japan*

[3]*Japan Atomic Energy Agency (in SPring-8), Sayo-cho, Sayo-gun, Hyogo 679-5148, Japan*

[4]*Nanostructures Research Laboratory, Japan Fine Ceramics Center, Nagoya 456-8587, Japan*

[5]*Center for Materials Research by Information Integration (CMI2), National Institute for Materials Science (NIMS), Tsukuba, Ibaraki 305-0047, Japan*

[6]*Office of the Vice President for Research, Shimane University, Matsue 690-8504, Japan*

(Received 3 October 2017; revised manuscript received 8 January 2018; published 31 January 2018)

Uniaxial ferroelectric $BaTi_2O_5$ with a Curie temperature T_C of 743 K was investigated to clarify its paraelectric-ferroelectric phase-transition behavior. The mechanism is discussed on the basis of the structure from short to long ranges determined by synchrotron x-ray diffraction and the lattice dynamics probed by Raman spectroscopy. $BaTi_2O_5$ is regarded as a homogeneous system, and the lattice dynamics can be interpreted by the selection rules and tensor properties of the homogeneous structure. Angle-resolved polarized Raman spectroscopy clearly shows that an *A*-mode-type overdamped phonon plays the key role in the phase transition. Using a combination of experimental results and first-principles calculations, we explain the phase transition as follows: In one of three TiO_6 octahedral units, Ti vibrates along the *b* axis opposite an oxygen octahedral unit with large damping in the paraelectric phase, whereas this vibration is frozen in the ferroelectric phase, leading to a change in the space group from nonpolar $C2/m$ to polar $C2$.

DOI: 10.1103/PhysRevB.97.024116

I. INTRODUCTION

Uniaxial ferroelectric $BaTi_2O_5$ shows a dielectric response with a dielectric constant ε_b of ∼25 000 at a Curie temperature T_C of ∼743 K, as shown in Fig. 1 [1–3]. At the paraelectric-ferroelectric phase transition, the crystal structure changes from paraelectric $C2/m$ to ferroelectric $C2$ with spontaneous polarization along the *b* axis [4,5]. Because the phase-transition-induced dielectric response of $BaTi_2O_5$ is stronger at higher Curie temperature than that of the most-typical capacitor material $BaTiO_3$, which exhibits a dielectric constant ε_C of ∼10 000 at a T_C of ∼410 K, $BaTi_2O_5$ has attracted renewed interest for high-temperature applications since the discovery of its ferroelectricity [6–11]. In addition, piezoelectric coefficients comparable with those of $PbTiO_3$ have been predicted by first-principles calculations, indicating that $BaTi_2O_5$ is a candidate end-member for lead-free piezoelectric solid-solution materials [12]. The properties of Pb-based ferroelectrics with high dielectric and piezoelectric responses are closely related to their phase transition and phase diagram [13–17]; therefore, understanding the paraelectric-ferroelectric phase transition and the characteristics of each phase is the key to developing next-generation $BaTi_2O_5$-based materials for high-temperature capacitors and for lead-free piezoelectrics.

From a microscopic viewpoint, the difference between the paraelectric and ferroelectric phases is characterized by TiO_6 octahedral units; one of the three Ti sites (Ti1) shifts in the opposite direction from the O in the TiO_6 octahedral unit, giving rise to ferroelectricity, whereas the other two Ti sites (Ti2 and Ti3) and their corresponding O atoms shift in the same direction [3–5,9]. Despite extensive studies of $BaTi_2O_5$, the mechanism of its phase transition remains controversial. Because of the critical slowing of one relaxation observed in low-frequency inelastic light scattering, Hushur *et al.* attributed the mechanism to an order-disorder type, where Ti hops in two equivalent off-center positions in the paraelectric phase but is trapped at one of them in the ferroelectric phase [18]. By contrast, on the basis of a structural study by synchrotron x-ray powder diffraction, Moriyoshi *et al.* reported that the mean-square thermal displacement of Ti1 is larger than those of Ti2 and Ti3 and that off-centering of Ti1 was not observed [19]. The results of Moriyoshi *et al.* indicate that the phase transition originates from a displacive-type mechanism, where one optical phonon in a paraelectric phase slows as the temperature approaches T_C at the Γ point. That is, one vibration pattern freezes at temperatures below T_C; as a result, a static polar displacement appears in the ferroelectric phase. What appears to be lacking is interpretation of the quasielastic scattering in the low-frequency inelastic light-scattering spectrum. Quasielastic scattering indicates dynamic movements in materials and can originate from entropy and phonon fluctuations, degenerate electronic levels, phasons, ion hopping and tunneling, reorientation of precursor clusters, and overdamped lattice vibrations. In cases where quasielastic scattering is related to a ferroelectric phase transition, the possibilities of ion hopping and tunneling, reorientation of precursor clusters, and overdamped phonons are usually considered because freezing

*tsukada@edu.shimane-u.ac.jp

†yfujii@fc.ritsumei.ac.jp

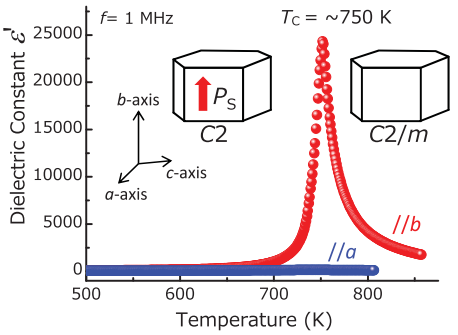

FIG. 1. Dielectric constant ε' of $BaTi_2O_5$ as a function of temperature [1,2]. The ε' along the b axis is enhanced at T_C, whereas no anomaly is observed for ε' along the a axis. Inset: Forms of crystals and the relationship with crystallographic axes. The spontaneous polarization P_S appears along the b axis.

of each motion leads to structural changes. For example, in Pb-based relaxor ferroelectrics, the quasielastic scattering is attributed to reorientation of an inhomogeneous structure referred to as the polar nanoregion; this structure differs from the macroscopic structure [20,21]. The inhomogeneous structure violates the selection rules for light scattering; thus, careful investigations from both local and macroscopic viewpoints are essential to understanding the behaviors of ferroelectric materials [22–25]. Thus, at the present stage of understanding of $BaTi_2O_5$, investigations of the structure from short to long ranges and the dynamics, including its direction dependence, are necessary to understand the phase-transition mechanism and the properties of each phase. Herein, the assignment of quasielastic light scattering is the key to solving the controversy on the phase transition. Light scattering from optical phonons depends on Raman tensors directly obtained from the point symmetry of crystals; thus Raman scattering measurements at different scattering geometries enable us to assign modes. However, there is a difficulty in changing scattering geometries since it usually needs repositioning of optical elements in a measurement system. One powerful technique to overcome the difficulty is angle-resolved polarized Raman spectroscopy in which a half-wave plate in the microscope changes the polarization direction of incident and scattered light [26]. Without a significant change in optical system, a 2×2 matrix in Raman tensors can be probed by just rotating the half-wave plate.

In this study, we conducted synchrotron x-ray powder diffraction (XRD) experiments on $BaTi_2O_5$ and showed the pair distribution function (PDF) to investigate the appearance of an inhomogeneous structure whose dynamics may be an origin of quasielastic scattering. Because the result showed that $BaTi_2O_5$ is homogeneous, we further conducted angle-resolved polarized Raman scattering measurements and assigned each peak in the spectra on the basis of Raman tensors of the determined homogeneous structure. The angle dependence indicates that quasielastic scattering originates from an overdamped A mode implying that ferroelectric phase transition in $BaTi_2O_5$ can be categorized as displacive type with large damping of the soft phonon mode. The experimental results are interpreted in detail using first-principles calculations, and the displacement pattern related to the overdamped A mode is determined.

II. EXPERIMENTS

Single crystals of $BaTi_2O_5$ for angle-resolved Raman spectroscopy were grown from a melt of $BaTiO_3$ (Kishida Chemical) and TiO_2 (Sigma-Aldrich Chemistry) starting from 1659 K [1]. The crystals were needlelike along the b axis and exhibited a hexagonal column shape, where a surfaces (100) were obtained, as shown in Fig. 1. Powders of $BaTi_2O_5$ for synchrotron XRD and temperature-dependent Raman scattering measurements were fabricated from $BaCO_3$ (Sakai Chemical) and TiO_2 (Showa Denko) using solid-state reactions; the fabrication process is described elsewhere [27].

Synchrotron XRD data were collected at 300 K using 60-keV incident x rays at the BL14B01 beamline in SPring-8. The structural parameters of the obtained materials were refined by Rietveld profile fitting using the RIETAN-FP program [28]. This method enabled us to determine the average (or macroscopic) structure. Crystal structures were drawn using VESTA [29]. The experimental PDF, $G(r)$, was obtained by taking the Fourier transform of the reduced structure factor $F(Q)$ [30]. The PDF describes the number density of interatomic pair distances as a function of distance r. The short-range order can be modeled exactly using the PDF. The fitting was carried out using PDFFIT2 and PDFGUI [31] under the constraint of space group $C2$; the parameters determined by the Rietveld refinement were adopted as initial parameters.

Raman scattering was measured using our own system composed of a polarization rotation system installed in a microscope. A schematic of the setup is shown in Fig. 2(a). A $BaTi_2O_5$ crystal or powders were placed inside a temperature-controlled cell (Linkam) on an xyz mapping stage (Tokyo Instruments) installed in the microscope (Olympus). Linearly polarized incident light from a diode-pumped solid-state laser (Spectra Physics) with single-frequency operation at 532 nm and a power of 200 mW traveled to the sample through a polarization rotation device (Sigma Koki) [26] equipped with a broadband half-wave plate (Kogakugiken) in the microscope. The strong elastic scattering was eliminated by two volume Bragg gratings—so-called "ultranarrow-band notch filters" (OptiGrate). The refractive index of the volume Bragg gratings varies periodically, which generates a dielectric mirror for one specific wavelength. The inelastic scattering light was dispersed by a single monochromator (Lucir), and the dispersed component was detected using a charge-coupled device (Andor). The concept of polarization rotation in the microscope is shown in Fig. 2(b). When the polarization direction of incident light is inclined $\theta/2$ with respect to the optical axis of the wave plate which rotates the polarization plane of incidence by θ. However, the polarization direction of scattering light, propagating in the direction opposite the incident light, is rotated by $-\theta$. Thus, θ-directed incident light was focused on the sample and light was scattered according to the Raman polarizability. Because of the polarizer, the scattering can be divided into the θ direction [horizontal-horizontal (HH)] and the $(\theta+\pi/2)$ direction [horizontal-vertical (HV)]. The θ dependence of Raman scattering intensity provides information about the Raman tensor elements, which can be used to probe the dynamical properties and point symmetry of materials [26]. The θ dependence of Raman scattering has usually been measured with rotation of the sample; i.e., the measurements were

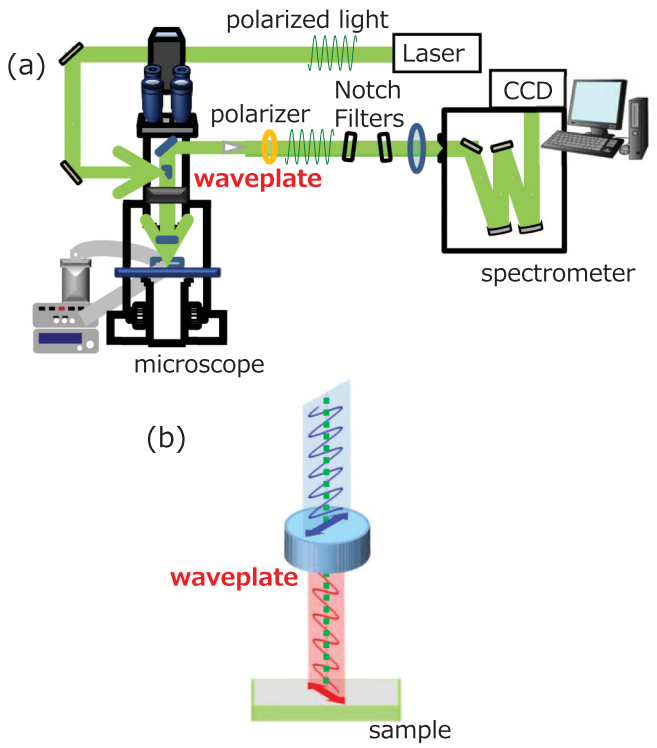

FIG. 2. (a) Schematic of the experimental setup. A sample is irradiated with incident light on the *xyz* mapping stage. The strong elastic scattering is eliminated by ultranarrow-band notch filters. The Raman scattering is dispersed by a single monochromator and is detected using a CCD. (b) Polarization rotation through a half-wave plate [26]. To rotate the polarization of the incident and the scattering light, a computer-controlled half-wave plate is installed in the microscope.

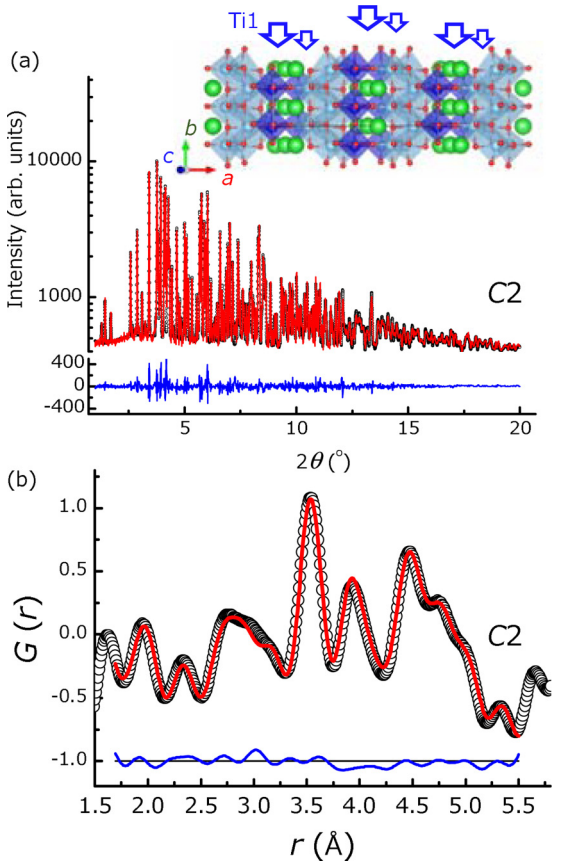

FIG. 3. (a) Synchrotron x-ray diffraction pattern of $BaTi_2O_5$ measured at 300 K (ferroelectric phase). The energy of the incident x rays was 60 keV. Rietveld profile fitting was performed by assuming a $C2$ monoclinic structure. $R_{WP} = 5.407\%$, $R_P = 3.701\%$, and $S = 1.4706$. The deviation between the observed intensities (○) and calculated intensities (solid line) is plotted at the bottom. The crystal structure obtained by Rietveld profile fitting is shown in the inset. (b) PDF, $G(r)$, transformed from $F(Q)$. The fitting was performed by the assumption of a $C2$ space group and using internal coordinates determined by Rietveld profile fitting.

performed only at room temperature [25,32]. However, our angle-resolved polarized Raman spectroscopy method enables us to measure them in a wide frequency region even at high temperatures, which is important for our study of phase transitions.

First-principles calculations were carried out using the projector-augmented wave (PAW) method within density functional theory [33], as implemented in the VASP code [34,35]. The generalized gradient approximation with Perdew-Burke-Ernzerhof revised for solids (GGA-PBE_sol) was used for the exchange-correlation functional [36]. Using the PAW method, $5s$, $5p$, and $6s$ electrons for Ba; $3s$, $3p$, $3d$ and $4s$ electrons for Ti; and $2s$ and $2p$ electrons for O were treated explicitly as valence electrons. The plane-wave cutoff was set at 500 eV, and the size of the k-point mesh for Brillouin zone sampling of primitive cells, based on the Γ-point-centered Monkhorst-Pack scheme [37], was $8\times8\times2$ for monoclinic ($C2/m$ and $C2$) unit cells containing 24 atoms. Lattice constants and internal coordinates were fully optimized until residual Hellmann-Feynman (HF) forces were smaller than 1.0×10^{-3} eV/Å while the symmetry constraints of the given space group were maintained. Dynamical properties were computed from interatomic force constants in real space. The entire set of force constants was obtained from HF forces generated by nonequivalent atomic displacements in a supercell of a given crystal structure. All lattice dynamics calculations were performed with the PHONON code [38]. In an ionic crystal, dipole-dipole interactions affect interatomic force constants and cause longitudinal optical/transverse optical (LO/TO) splitting when wave vector $k \approx 0$, i.e., near the Γ point. In this study, however, we did not take into account the influence of the dipole on the interatomic force constants because we were interested primarily in identifying soft-mode phonons. The inclusion of the LO/TO splitting has only a slight effect on soft-mode phonons because the dipole-dipole interaction is limited to LO modes when $k \approx 0$, leaving the frequencies of TO modes unchanged.

III. RESULTS AND DISCUSSION

Figure 3(a) presents the synchrotron XRD pattern for the $BaTi_2O_5$ powder at 300 K. The Rietveld profile fitting results for the ferroelectric phase are also shown. The reliability factors (R factors) of the fitting results are small; thus the fitting is considered to be good. The structural parameters are found to be in good agreement with those previously reported for a monoclinic $C2$ space group structure [4,5,9]. Figure 3(b) shows

TABLE I. Raman activity of phonon modes in the paraelectric and ferroelectric phases. (R) denotes a Raman active mode.

$C2/m$	$C2$
$A_g(R)$	$A\,(R)$
A_u	$A\,(R)$
$B_g(R)$	$B\,(R)$
B_u	$B\,(R)$

the PDF obtained from the XRD pattern. It shows sharp peaks, which represent interatomic distances. For example, the peak at approximately 3.92 Å is attributed to interatomic distances corresponding to the lattice parameter along the b axis. Starting from the parameters obtained by Rietveld refinement, this short-range structure was well fitted to a $C2$ space group. This result indicates that no inhomogeneous structure is present; that is, the macroscopic properties can be explained by the behaviors of the unit cell and the internal coordinates, as shown in Fig. 3(a), which depicts the long-range crystal structure obtained by Rietveld refinement. As mentioned in the Introduction, the structural analysis shows that Ti1 shifts in the opposite direction from the O in the TiO_6 octahedral unit along the b axis, giving rise to ferroelectricity.

The XRD results differ from those reported in previous studies for Pb-based relaxor ferroelectrics and $BaTiO_3$ containing inhomogeneous structures [22,24,30], where mode assignments of Raman scattering are difficult due to various structures exhibiting different Raman activities [23,25]. However, because our structural analysis shows that the $BaTi_2O_5$ can be regarded as a homogeneous system, the Raman activity can be predicted on the basis of the selection rules of the single structure. Table I shows the Raman activities of both the paraelectric and the ferroelectric phases of $BaTi_2O_5$. The structural parameters reported by Moriyoshi *et al.* [19] were used for the calculation of the paraelectric phase, whereas those in Fig. 3(a) were used for the calculation of the ferroelectric phase. All phonon modes in the paraelectric phase were classified into one of four types; two of the modes are Raman active, whereas the other two modes are not. By contrast, in the case of the ferroelectric phase, the number of modes was reduced by the structural change and all of the phonon modes were Raman active.

Figure 4(a) shows the Raman spectra of powdered samples at several temperatures. Numerous sharp peaks originating from the phonon modes were observed. The observed peaks were fitted using a Lorentzian function; the temperature dependence of the peak frequencies below 170 cm^{-1} are shown in Fig. 4(b). The sharp phonon peaks exhibited no anomalies at T_C. However, quasielastic scattering became strong at temperatures around T_C. Because the width of quasielastic scattering is as narrow as 1 cm^{-1}, our grating spectrometer lacks sufficient resolution to acquire valid values. Therefore, the width of the quasielastic scattering obtained using a Fabry-Perot interferometer (Brillouin spectroscopy) [18] is shown in Fig. 4(b), where the width becomes narrowest at T_C. This result indicates that the movement pattern corresponding to the quasielastic scattering freezes at T_C and that the freezing induces ferroelectricity in $BaTi_2O_5$. Although the observed number of peaks is less than that predicted by the factor group analysis on the crystal structure [19], where there are $34A + 35B$ Raman active modes in the ferroelectric phase and $12A_g + 24B_g$ Raman active modes in the paraelectric phase, due to the insufficient resolution of the spectrometer [39], marked changes should be shown in the spectra if there is a softening peak to induce the phase transition.

Here we closely examine the Raman scattering from $BaTi_2O_5$. Because no inhomogeneous structure was observed, Raman scattering from crystalline $BaTi_2O_5$ can be represented by Raman tensors, $\mathfrak{R}$, determined from the crystal structure. The Raman scattering intensity I for each phonon mode is proportional to

$$I \propto |e_s \cdot \mathfrak{R} \cdot e_i|^2, \tag{1}$$

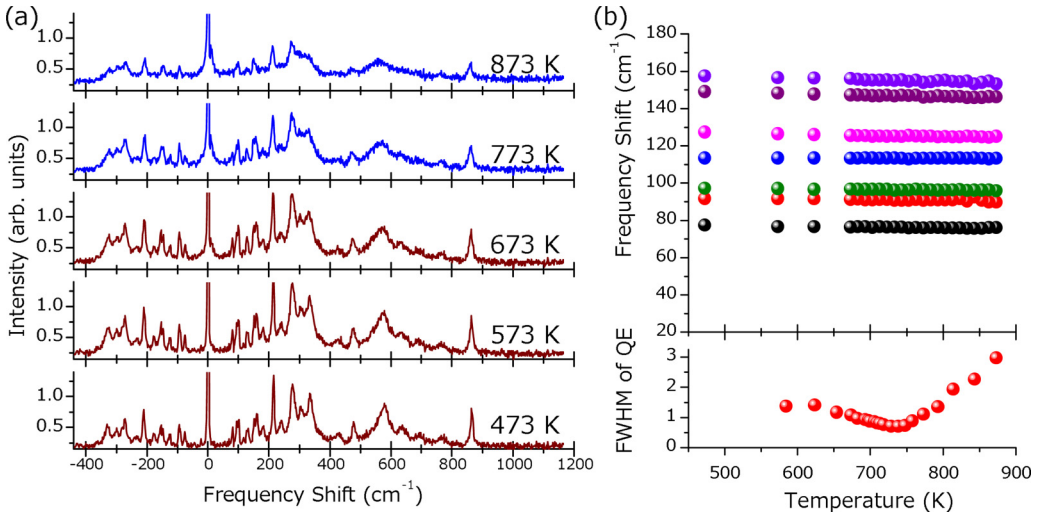

FIG. 4. (a) Raman spectra of $BaTi_2O_5$ powders at five temperatures. Notch filters shown in Fig. 2(a) suppress the intensity between -6 cm^{-1} and 6 cm^{-1}. The small dip at 6 cm^{-1} is the result of the suppression and is not an intrinsic peak. (b) Temperature dependence of the frequency shift of Raman scattering determined by fitting. The width of quasielastic scattering was obtained from Ref. [18].

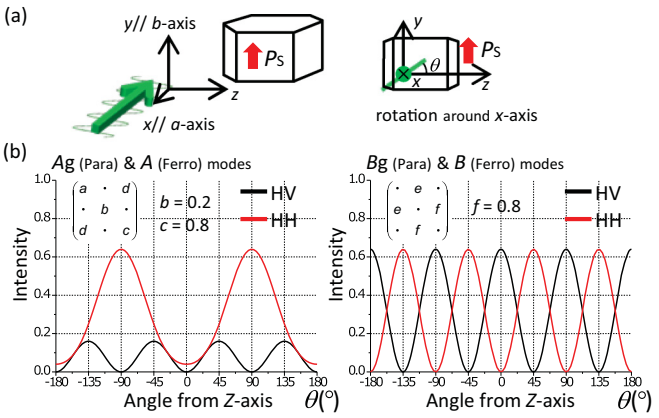

FIG. 5. (a) Relationship between the laboratory system and crystallographic axes of $BaTi_2O_5$. (b) Calculated polarization angle dependence of Raman intensity in the horizontal-horizontal (HH) and horizontal-vertical (HV) geometries for $C2/m$ (paraelectric) and $C2$ (ferroelectric) structures of $BaTi_2O_5$ according to Eqs. (4) and (5) under the values $b = 0.2$, $c = 0.8$, and $f = 0.8$.

where e_i and e_s denote unit vectors in the incident and scattered directions, respectively. In this study, we set (010) for e_i and (010) as the HH configuration or (001) as the HV configuration for e_s. As shown in Table I, Raman scattering from $BaTi_2O_5$ can be assigned as A_g or B_g in the paraelectric phase and as A or B in the ferroelectric phase, with the following tensors:

$$\begin{pmatrix} a & \cdot & d \\ \cdot & b & \cdot \\ d & \cdot & c \end{pmatrix} \quad \text{for } A \text{ - type modes,}$$

$$\begin{pmatrix} \cdot & e & \cdot \\ e & \cdot & f \\ \cdot & f & \cdot \end{pmatrix} \quad \text{for } B \text{ - type modes.} \tag{2}$$

The tensor quantities indicate that the Raman scattering intensity should depend on the polarization direction of the incident and scattered lights and on the scattering geometry. In the present study, we assigned the peaks by rotating the angle of the polarization direction of the incident light and the scattered light, θ, under backscattering geometry. We set the crystalline sample as shown in Fig. 5(a). Using a rotation matrix,

$$R = \begin{pmatrix} 1 & \cdot & \cdot \\ \cdot & \cos\theta & -\sin\theta \\ \cdot & \sin\theta & \cos\theta \end{pmatrix}. \tag{3}$$

Raman tensors in the microscope at θ are transformed to

$$\Re' = R^{-1} \cdot \Re \cdot R. \tag{4}$$

Thus, through Eqs. (1)–(4), the Raman intensities for A-type modes are given by

$$I(\mathrm{HH}) \propto (b\cos^2\theta + c\sin^2\theta)^2 \quad \text{and}$$
$$I(\mathrm{HV}) \propto \left(\frac{-b+c}{2}\sin 2\theta\right)^2, \tag{5}$$

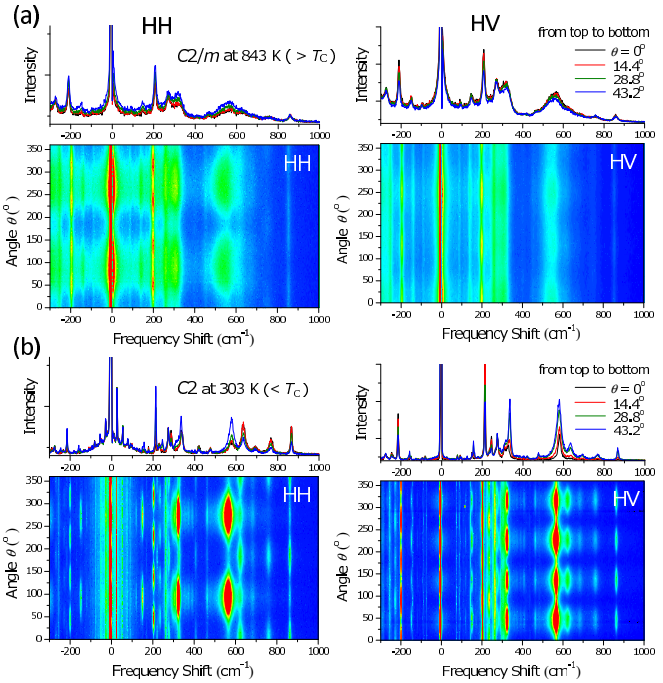

FIG. 6. Angle-resolved polarized Raman spectra and the contour maps of $BaTi_2O_5$ crystal in (a) the paraelectric phase at 843 K and in (b) the ferroelectric phase at 303 K.

respectively, whereas those for B-type modes are given by

$$I(\mathrm{HH}) \propto (f\sin 2\theta)^2 \quad \text{and}$$
$$I(\mathrm{HV}) \propto (f\cos 2\theta)^2, \tag{6}$$

respectively. The θ dependence of the Raman scattering intensity from $BaTi_2O_5$ is expected to depend on the Raman tensors, as demonstrated in Fig. 5(b), which shows a clear difference between modes in the HH scattering geometry. The angle-resolved Raman spectra collected at a temperature just above T_C and at approximately room temperature are shown in Fig. 6. Each Raman peak is θ dependent; by comparison with Fig. 5(b), peaks with two maxima in the θ dependence under the HH scattering geometry (89, 150, 270, 330, 460, and 550 cm^{-1}) belong to the A-type mode, whereas peaks with four maxima (210, 230, and 635 cm^{-1}) belong to the B-type mode in Eq. (2). Notably, the A-type mode shows flatter θ dependence near T_C than that at 303 K due to the increase in b/c in the Raman tensor. Here the quasielastic scattering apparently behaves similarly to the A-type mode, which indicates that quasielastic scattering originates from an overdamped phonon. However, modes related with ferroelectric phase transition should be polar; the appearance is prohibited for the symmetry restriction. It can be a result of symmetry breaking due to the large enough correlation length near the T_C. Thus, at the present stage, we attribute the quasielastic scattering to the overdamped A_u mode in the paraelectric phase and the A mode in the ferroelectric phase.

The concept of an overdamped phonon is based on harmonic vibration with large damping. When the damping Γ becomes much larger than the vibration frequency ω_0, the vibration in the Raman spectrum appears to be the zero-centered

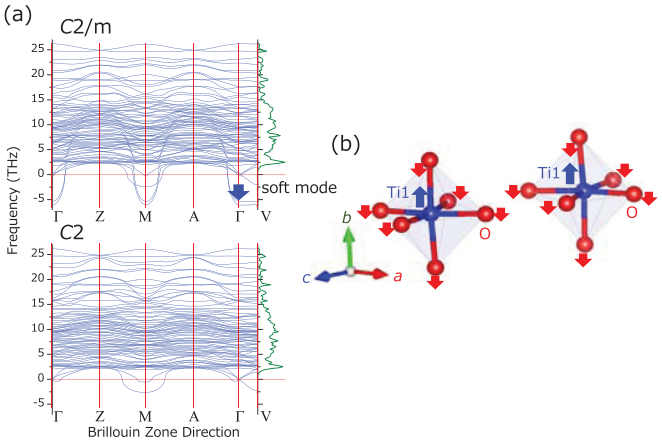

FIG. 7. (a) Phonon dispersion curves above and below T_C, as obtained by first-principles calculations. A solid arrow at the Γ point in the paraelectric phase denotes the soft mode that condensates toward T_C. (b) Displacement pattern of the soft mode.

Lorentzian-type peak known as quasielastic scattering. In this case, the quasielastic scattering vibration is indistinguishable from a relaxation process with relaxation time $\tau = \Gamma/\omega_0^2$, which is the key to resolving the discrepancy concerning the interpretation of the phase-transition mechanism mentioned in the Introduction: Light spectroscopy indicates the phase transition is order-disorder type; however, local sites in the paraelectric phase, which are characteristic of that type, are not observed. Therefore, the phase transition of $BaTi_2O_5$ is classified as displacive type with a soft optical phonon. However, the damping of the soft phonon is sufficiently large for the transition to also be interpreted as order-disorder type, where relaxation shows critical slowing as the temperature approaches T_C.

To clarify the vibration pattern of the overdamped soft optical phonon, we carried out first-principles calculations for $BaTi_2O_5$. Figure 7(a) shows the phonon dispersion curves. Two unstable modes at the Γ and M points in the paraelectric phase and one mode at the Γ point in the ferroelectric phase are removed. The change in the phonon dispersion curves at T_C is common because proper ferroelectric phase transitions should be induced by the condensation of one phonon at the Γ point. The ferroelectric phase was 14.05 meV/f.u. more stable than the paraelectric phase as a result of the softening phonon at the Γ point. The displacement pattern of the mode is depicted in Fig. 7(b). If the phonon freezes below T_C, the ferroelectric phase appears. Here, the displacement pattern is consistent with the change in the crystal structure [4,5,19]. Notably, the Ti1-O_6 octahedral unit in $BaTi_2O_5$ resembles that in the polar tetragonal phase of $BaTiO_3$ with $P4mm$ as an average structure.

In summary, in the mechanism of the phase transition of $BaTi_2O_5$ from paraelectric $C2/m$ to ferroelectric $C2$, the system is homogeneous and one phonon with the displacement pattern shown in Fig. 7(b) freezes below T_C. The damping of the vibration is so large that distinguishing vibration from relaxation is difficult, which led to the previous controversy concerning the mechanism.

IV. SUMMARY

In summary, we have characterized the static and dynamic properties of high-T_C $BaTi_2O_5$ using synchrotron XRD and Raman scattering experiments. The structure of $BaTi_2O_5$ is homogeneous, unlike that of $BaTiO_3$, and one of three Ti sites (Ti1) shifts along the b axis opposite an oxygen octahedral unit at temperatures below T_C. The temperature dependence of Raman scattering shows no change at T_C except quasielastic scattering, which indicates that quasielastic scattering plays the main role in the enhancement of the dielectric constant at T_C. Due to the homogeneous monoclinic structure, the quasielastic scattering was interpreted on the basis of Raman tensors: The quasielastic scattering is attributed to the A_u mode in the paraelectric phase and to the A mode in the ferroelectric phase, as determined by angle-resolved Raman spectroscopy, which enables us to measure light-polarization-direction dependence of Raman scattering in a wide frequency region at various temperatures. These results indicate that ferroelectric phase transition of $BaTi_2O_5$ is categorized as displacive type with large damping of the soft A_u mode. The displacement pattern of the mode was determined by first-principles calculations to describe from in a microscopic viewpoint. Understanding of the phase-transition behavior of high-T_C $BaTi_2O_5$ gives rise to an enormous number of potential applications of this material in high-performance capacitors and lead-free actuators and might help overcome the high-operation-temperature limit of dielectric tips.

ACKNOWLEDGMENTS

We would like to thank M. Iwata for his comments on Raman scattering and M. Sota and K. Nonomura for their assistance with fabricating the $BaTi_2O_5$ powders. A part of this work was performed under the Shared Use Program of JAEA Facilities (Grant No. 2016A-E3620) with the approval of the Nanotechnology Platform project supported by MEXT, Japan (Grant No. A-16-AE-3620). The synchrotron radiation experiments were performed at JAEA beamline BL14B01 in SPring-8 (No.2016A3620). This work was partly supported by JSPS KAKENHI Grant No. 16K04931.

[1] Y. Akishige, K. Fukano, and H. Shigematsu, Jpn. J. Appl. Phys. **42**, L946 (2003).
[2] Y. Akishige, H. Shigematsu, A. Kitahara, and I. Takahashi, J. Korean Phys. Soc. **46**, 24 (2005).
[3] T. Akashi, H. Iwata, and T. Goto, Mater. Trans. **44**, 802 (2003).
[4] M. Yashima, R. Tu, T. Goto, and H. Yamane, Appl. Phys. Lett. **87**, 101909 (2005).
[5] H. Shigematsu, Y. Akishige, S. Gvasaliya, V. Pomjakushin, S. Lushnikov, and S. Kojima, Ferroelectrics **346**, 43 (2007).

[6] J. Yu, Y. Arai, T. Masaki, T. Ishikawa, S. Yoda, S. Kohara, H. Taniguchi, M. Itoh, and Y. Kuroiwa, Chem. Mater. **18**, 2169 (2006).
[7] J. Zhang, J. Yu, M. Chao, E. Liang, M. Li, and D. Li, J. Mater. Sci. **47**, 1554 (2012).
[8] N. Zhu and A. R. West, J. Am. Ceram. Soc. **93**, 295 (2010).
[9] C. Moriyoshi, Y. Kuroiwa, A. Masuno, and H. Inoue, J. Phys. Soc. Jpn. **81**, 014706 (2012).
[10] W. Liu, S. Tsukada, and Y. Akishige, Jpn. J. Appl. Phys. **53**, 05FE03 (2014).
[11] J. Xu and Y. Akishige, Appl. Phys. Lett. **92**, 52902 (2008).
[12] U. Waghmare, M. H. F. Sluiter, T. Kimura, T. Goto, and Y. Kawazoe, Appl. Phys. Lett. **84**, 4917 (2004).
[13] G. Smolensky, J. Phys. Soc. Jpn. Suppl. **28**, 26 (1970).
[14] B. Noheda, D. E. Cox, G. Shirane, R. Guo, B. Jones, and L. E. Cross, Phys. Rev. B **63**, 014103 (2000).
[15] Z.-G. Ye, B. Noheda, M. Dong, D. Cox, and G. Shirane, Phys. Rev. B **64**, 184114 (2001).
[16] A. A. Bokov and Z. G. Ye, J. Mater. Sci. **41**, 31 (2006).
[17] S.-E. Park and T. R. Shrout, J. Appl. Phys. **82**, 1804 (1997).
[18] A. Hushur, H. Shigematsu, Y. Akishige, and S. Kojima, Appl. Phys. Lett. **86**, 112903 (2005).
[19] C. Moriyoshi, N. Okizaki, Y. Kuroiwa, J. Yu, Y. Arai, and A. Matsuno, Jpn. J. Appl. Phys. **48**, 09KF06 (2009).
[20] S. Tsukada and S. Kojima, Phys. Rev. B **78**, 144106 (2008).
[21] M. A. Helal, M. Aftabuzzaman, S. Tsukada, and S. Kojima, Sci. Rep. **7**, 44448 (2017).
[22] Y. Yoneda, K. Suzuya, J. Mizuki, and S. Kohara, J. Appl. Phys. **100**, 93521 (2006).
[23] I. G. Siny, S. G. Lushnikov, R. S. Katiyar, and E. A. Rogacheva, Phys. Rev. B **56**, 7962 (1997).
[24] I. K. Jeong, Phys. Rev. B **79**, 052101 (2009).
[25] H. Taniguchi, M. Itoh, and D. Fu, J. Raman Spectrosc. **42**, 706 (2011).
[26] Y. Fujii, M. Noju, T. Shimizu, H. Taniguchi, M. Itoh, and I. Nishio, Ferroelectrics **462**, 8 (2014).
[27] S. Tsukada and Y. Akishige (unpublished).
[28] F. Izumi and K. Momma, Solid State Phenom. **130**, 15 (2007).
[29] K. Momma and F. Izumi, J. Appl. Crystallogr. **44**, 1272 (2011).
[30] Y. Yoneda and S. Kohara, J. Korean Phys. Soc. **55**, 741 (2009).
[31] C. L. Farrow, P. Juhas, J. W. Liu, D. Bryndin, E. S. Božin, J. Bloch, T. Proffen, and S. J. L. Billinge, J. Phys.: Condens. Matter **19**, 335219 (2007).
[32] T. Livneh, J. Zhang, G. Cheng, and M. Moskovits, Phys. Rev. B **74**, 035320 (2006).
[33] P. E. Blöchl, Phys. Rev. B **50**, 17953 (1994).
[34] G. Kresse and J. Furthmüller, Phys. Rev. B **54**, 11169 (1996).
[35] G. Kresse and J. Furthmüller, Comput. Mater. Sci. **6**, 15 (1996).
[36] J. P. Perdew, A. Ruzsinszky, G. I. Csonka, O. A. Vydrov, G. E. Scuseria, L. A. Constantin, X. Zhou, and K. Burke, Phys. Rev. Lett. **100**, 136406 (2008).
[37] H. J. Monkhorst and J. D. Pack, Phys. Rev. B **13**, 5188 (1976).
[38] K. Parlinski, Y. Kawazoe, and Y. Waseda, J. Chem. Phys. **114**, 2395 (2001).
[39] A. Hushur, S. Kojima, H. Shigematsu, and Y. Akishige, J. Korean Phys. Soc. **46**, 86 (2005).